

# 1 **Mixed layer depth variability in the Red Sea**

2 Cheriyeri P. Abdulla<sup>1\*</sup>, Mohammed A. Alsaafani<sup>1,2</sup>, Turki M. Alraddadi<sup>1</sup>, and Alaa M. Albarakati<sup>1</sup>

3 <sup>1</sup>Department of Marine Physics, Faculty of Marine Sciences, King Abdulaziz University, Jeddah, Saudi Arabia.

4 <sup>2</sup>Department of Earth & Environmental Sciences, Faculty of Science, Sana'a University, Yemen.

5

6 *Correspondence to:* Cheriyeri P. Abdulla (acp@stu.kau.edu.sa)

7 **Abstract**

8 For the first time, a monthly climatology of mixed layer depth (MLD) in the Red Sea has been derived  
9 based on temperature profiles. The general pattern of MLD variability is clearly visible in the Red Sea,  
10 with deep MLDs during winter and shallow MLDs during summer. Transitional MLDs have been found  
11 during the spring and fall. Northern end of the Red Sea experienced deeper mixing and higher MLD,  
12 associated with the winter cooling of the high-saline surface waters. Further, the region north of 19°N  
13 experienced deep mixed layers, irrespective of the season. Wind stress plays a major role in the MLD  
14 variability of the southern Red Sea, while net heat flux and evaporation are the dominating factors in the  
15 central and northern Red Sea regions. Ocean eddies and Tokar gap winds significantly alters the MLD  
16 structure in the Red Sea. The dynamics associated with the Tokar gap winds leads to a difference of more  
17 than 20 m in the average MLD between the north and south of the Tokar axis.

18 **Keywords:** Mixed layer depth, Red Sea, Eddies, Tokar gap winds, Air-Sea interaction.

## 19 **1 Introduction**

20 The surface mixed layer is a striking and universal feature of the open ocean where the turbulence  
21 associated with various physical processes leads to the formation of a quasi-homogeneous layer with  
22 nearly uniform properties. The thickness of this layer, often named mixed layer depth (MLD), is one of  
23 the most important oceanographic parameters, as this layer directly communicates and exchanges energy  
24 with the atmosphere and therefore has a strong impact on the distribution of heat (Chen et al., 1994),  
25 ocean biology (Polovina et al., 1995) and near-surface acoustic propagation (Sutton et al., 2014). Heat  
26 and fresh-water exchanges at the air-sea interface and wind stress are the primary forces behind turbulent  
27 mixing. The loss of heat and/or freshwater from the ocean surface can weaken the stratification and  
28 enhance the mixing. Similarly, a gain in heat and/or freshwater can strengthen the stratification and reduce  
29 the mixing. The shear and stirring generated by the wind stress enhance the vertical mixing and play a  
30 major role in controlling the deepening of the oceanic mixed layer. Further, the stirring associated with  
31 turbulent eddies predominantly changes the mixing process, mainly along the isopycnal surfaces where  
32 stirring may occur with minimum energy (de Boyer Montegut et al., 2004; Hausmann et al., 2017; Kara  
33 et al., 2003).

34 The Red Sea is an important intermediate water formation region in the world ocean. Red Sea Outflow  
35 Water (RSOW), formed mainly due to open ocean convection in the northern Red Sea (Sofianos and  
36 Johns, 2002), propagates through Bab-el-Mandab to the Gulf of Aden (Alsaafani and Shenoi, 2007) and  
37 later spreads to the Indian Ocean. Its signature reaches into the south Indian Ocean about 6000 km away  
38 from the source (Beal et al., 2000). The Red Sea is surrounded by extremely hot arid lands and has a  
39 relatively strong evaporation rate ( $2 \text{ m yr}^{-1}$ ) with nearly zero precipitation (Albarakati and Ahmad, 2013;  
40 Bower and Farrar, 2015; Sofianos et al., 2002). This region experiences strong seasonality in its  
41 atmospheric forcing and buoyancy. These characteristics, along with the lack of river input, make the Red  
42 Sea one of the hottest and most saline ocean basin in the world. The narrow and semi-enclosed nature of  
43 the basin, the presence of multiple eddies, strong evaporation, lack of river input and very weak  
44 precipitation, seasonally reversing winds, etc. lead to complex dynamical processes in the Red Sea  
45 (Aboobacker et al., 2016; Yao et al., 2014a, 2014b; Zhai and Bower, 2013; Zhan et al., 2014).

46 The increase in number temperature and salinity profiles in recent years enhanced the study of MLD  
47 structure and its variability, both globally (de Boyer Montegut et al., 2004; Kara et al., 2003; Lorbacher  
48 et al., 2006) and regionally (Abdulla et al., 2016; D’Ortenzio et al., 2005; Keerthi et al., 2012, 2016; Zeng  
49 and Wang, 2017). The Red Sea has been investigated for many years with an emphasis on its different  
50 physical features, but there has been no detailed investigation on MLD variability, apart from a few  
51 studies addressing the hydrography and vertical mixing of localized areas (Alsaafani and Shenoi, 2004;  
52 Bower and Farrar, 2015; Carlson et al., 2014; Yao et al., 2014b).

53 In this work, an MLD climatology is produced for the first time based on in situ observations. Further,  
54 the roles of atmospheric forces and oceanic eddies on the changes of the MLD have been investigated.  
55 The following sections are arranged as: Sect. 2 describes the datasets used and methodology. The  
56 subsequent sections discuss the observed MLD variability in the Red Sea, the role of the major forces on  
57 the MLD variability, and the influence of Tokar gap winds. The main conclusions of the present work are  
58 given in the final section.

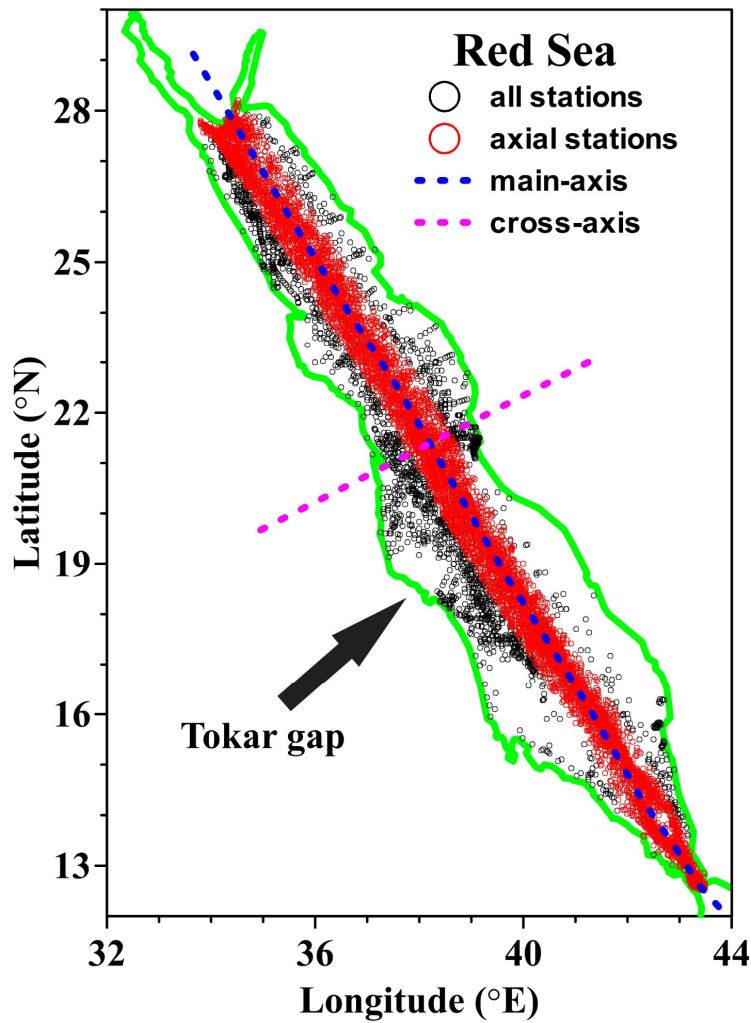
## 59 **2 Data and methods**

### 60 **2.1 Datasets**

61 Temperature and salinity profiles from different sources are collected, which are measured using CTD  
62 (conductivity-temperature-density profiler), PFL (autonomous profiling floats including ARGO floats),  
63 XBT (expendable-bathy-thermograph) and MBT (mechanical-bathy-thermograph). The World Ocean  
64 Database (<https://www.nodc.noaa.gov/OC5/SELECT/dbsearch/dbsearch.html>) is the main source. Apart  
65 from this, data from Coriolis data center ([http://www.coriolis.eu.org/Data-Products/Data-Delivery/Data-](http://www.coriolis.eu.org/Data-Products/Data-Delivery/Data-selection)  
66 [selection](http://www.coriolis.eu.org/Data-Products/Data-Delivery/Data-selection)) and several cruises conducted by individual institutions are also used in this analysis. The  
67 bathythermograph profiles were depth-corrected based on Cheng et al., (2014). A total 13,891 temperature  
68 profiles were made for the Red Sea (approximately 14 % of these profiles have salinity measurements)  
69 from 1934 to 2017.

70 These profiles are quality checked according to the procedure given in Boyer and Levitus (1994). In the  
71 duplicate check, all the profiles within a 1 km radius and taken on the same day are considered duplicates  
72 and are removed from the main dataset. The levels in the profile with large inversions in temperature  
73 (inversion  $\geq 0.3^{\circ}\text{C}$ ) are flagged and removed. If three or more inversions are present, then the entire  
74 profile is removed. The levels with extreme gradients  $\geq 0.7^{\circ}\text{C}$  are also removed from the profile. Since  
75 the present work is more focused on the changes in the upper layer of the ocean (from the surface to a  
76 150 m depth), profiles with low resolutions in the upper layers are removed. Almost 50 % of the profiles  
77 have resolutions of  $< 5$  m, while 7 % of the profiles have poor resolutions (resolutions of  $> 25$  m).

78 Out of the total of 13,891 profiles analysed, 11,212 profiles passed the quality check from CTD (690),  
79 PFL (1385), XBT (5507) and MBT (3630), and the spread is shown in Fig. 1. More than 80 % of these  
80 profiles are positioned along the middle of the Red Sea, with a sufficient number of profiles for each  
81 month (Fig. S1). The yearly and monthly distributions of the temperature profiles lie along the middle of  
82 the Red Sea and are given in the supplementary material (Fig. S2-S3). As part of the quality check, 2679  
83 profiles were removed from the main dataset. A total of 2063 salinity profiles are available for the entire  
84 Red Sea (Fig. S4). MLD is estimated based on the temperature profiles due to the increased number and  
85 sufficient monthly coverage comparing to that of salinity. The distribution of the temperature profiles  
86 used in this analysis is shown in Fig. 1.



87

88 **Figure 1.** The locations of temperature profiles in the Red Sea. Black circles denote all available profiles,  
 89 while red circles denote the profiles close to the main-axis that used for climatology calculation. The blue  
 90 (magenta) dashed line indicate main-axis (cross-axis) of the Red Sea.

91 The monthly mean values of heat fluxes and wind stress data are provided by Tropflux at a  $1^\circ \times 1^\circ$  spatial  
 92 resolution for the period 1979-2016, which are used to check the influence on MLD variability  
 93 ([http://www.incois.gov.in/tropflux\\_datasets/data/monthly/](http://www.incois.gov.in/tropflux_datasets/data/monthly/)). Tropflux captures better variability and less  
 94 bias than the other available fluxes and wind stress products (Praveen Kumar et al., 2012, 2013). Since  
 95 evaporation is not provided by Tropflux, the monthly mean values of evaporation from OAflux (from

96 1979 to 2016 and  $1^{\circ} \times 1^{\circ}$  spatial resolution) are used  
97 ([ftp://ftp.who.edu/pub/science/oaflux/data\\_v3/monthly/evaporation/](ftp://ftp.who.edu/pub/science/oaflux/data_v3/monthly/evaporation/)). The TRMM (Tropical rainfall  
98 measuring mission, <https://pmm.nasa.gov/data-access/downloads/trmm>) satellite provided the  
99 precipitation information for every  $0.25^{\circ} \times 0.25^{\circ}$  grid and 3-hourly to monthly time scale from 1997 to  
100 2016 (TRMM monthly 3B43\_V7 product is used). Monthly climatology of heat flux, evaporation,  
101 precipitation and wind stress are calculated. The period of precipitation data used for climatology  
102 calculation is shorter than other parameters. The present analysis is focusing on the seasonal timescale,  
103 and therefore, shorter data period will not significantly affect the results.

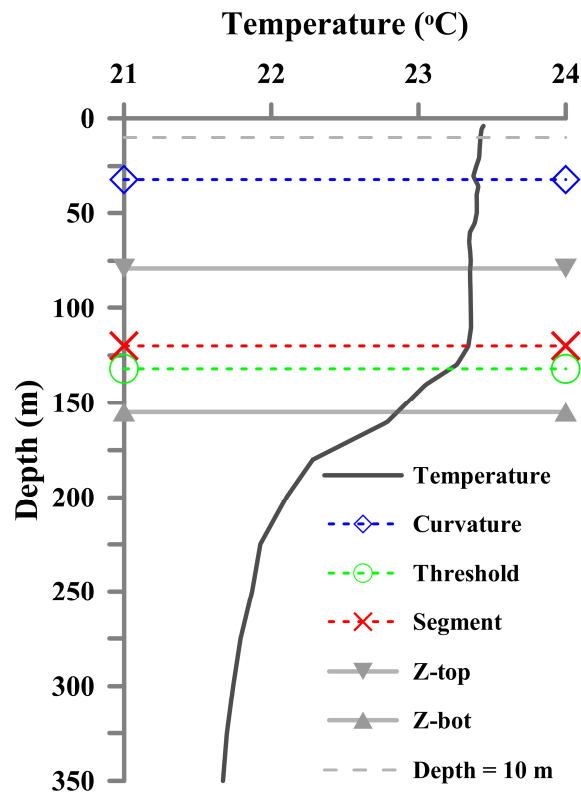
104 The daily sea level anomaly (SLA) maps are provided by AVISO ([www.aviso.oceanobs.com](http://www.aviso.oceanobs.com)). These data  
105 are the merged product of satellite estimates from TOPEX/Poseidon, Jason-1, ERS-1/2, and Envisat and  
106 are globally available with spatial resolution of  $0.25^{\circ} \times 0.25^{\circ}$  from the year 1992 to present (Ducet et al.,  
107 2000; LaTraon and Dibarboure, 1999). The SLA maps are used to describe the eddy distribution in the  
108 Red Sea. The merged data from all satellite estimates provides a general picture of SLA variability and  
109 the eddy distribution in the Red Sea, even though the number of satellite tracks passing through the narrow  
110 regions like Red Sea are relatively lower than the major ocean basins. Climate Forecast System Reanalysis  
111 (CFSR, <https://rda.ucar.edu/datasets/ds093.1/#!access>) provided hourly wind product from 1979 to 2010  
112 at a resolution of  $0.312^{\circ} \times 0.312^{\circ}$  grid (Saha et al., 2010) which is validated in the Red Sea (Aboobacker  
113 et al., 2016; Shanas et al., 2017). CFSR hourly wind at 10 m above the surface is used to study the Tokar  
114 gap winds.

## 115 **2.2 Methods**

116 The MLD can be estimated based on different methods. The Fig.2 shows a sample temperature profile  
117 collected on 19<sup>th</sup> January 2015 from Red Sea ( $24.9^{\circ}\text{N}$ ,  $35.18^{\circ}\text{E}$ ), with short-range gradients within the  
118 mixed layer. This gradient could rise from instrumental errors or turbulence in the upper layer. The  
119 curvature method (Lorbacher et al., 2006) identified MLD at 32 m, due to the presence of a short-range  
120 gradient at this depth. The threshold method (de Boyer Montegut et al., 2004) detected MLD at 130 m  
121 (threshold =  $0.2^{\circ}\text{C}$ ), while the segment method (Abdulla et al., 2016) identified MLD at 120 m. The

122 segment method based MLD could be considered as a reliable estimate comparing to both curvature  
123 (underestimation) and threshold method (overestimation). The segment method first identifies the portion  
124 of the profile with significant inhomogeneity where the transition from a homogeneous layer to  
125 inhomogeneous layer occurs. Then, this portion of the profile is analyzed to determine the MLD (detailed  
126 procedure of the estimation technique is given Abdulla et al., 2016). In the present study, MLD is  
127 estimated based on the segment method, which is found to be less sensitive to short-range disturbances  
128 within the mixed layer (Abdulla et al., 2016).

129



130

131 **Figure 2.** The MLD estimated for a sample temperature profile based on curvature, threshold, and  
132 segment methods. The Z-top and Z-bot respectively represent the top and bottom ends of the portion of  
133 the profile with significant inhomogeneity.



134 The availability of profiles is denser along the middle of Red Sea during all months. The present analysis  
135 is performed for the profiles that fall within 0.5 degrees to the east and west of the main axis that, running  
136 along almost the middle of the Red Sea (hereafter called the “main axis”), has the advantage of a sufficient  
137 number of profiles for every month. The main axis of the Red Sea is inclined to the west, with respect to  
138 true north, by ~30 degrees. For this reason, instead of zonally averaging, the climatology is calculated by  
139 averaging the MLDs in an inclined direction parallel to the “cross-axis” (Fig. 1). The MLD is estimated  
140 for the individual profiles, and then, the monthly climatology is calculated every 0.5° from south to north  
141 (13°N to 27.5°N).

142 The heat flux, evaporation, precipitation and wind stress are interpolated to 0.5°x0.5° spatial grid to match  
143 with MLD climatology with the help of climate data operator (CDO) tool available at  
144 <http://www.mpimet.mpg.de/cdo>. The change in surface water buoyancy forces is calculated following  
145 (Turner, 1973)

$$146 \quad B_0 = (C_p^{-1}g \alpha \rho_0^{-1}Q_{net}) + (-1 * g\beta s(E - P)) = B_{0T} + B_{0H} \quad (1)$$

147 where  $C_p$  = water heat capacity,  $g$  = acceleration due to gravity,  $\alpha$ =thermal expansion coefficient,  $\rho_0$  =  
148 density of surface water,  $Q_{net}$ = net heat flux at the sea surface,  $\beta$  = haline contraction coefficient,  $s$ =salinity  
149 of surface water,  $E$  = evaporation rate, and  $P$  = precipitation. In Eq. (1),  $B_{0T}$  and  $B_{0H}$ , respectively, represent  
150 the thermal and haline components of the buoyancy force. For ease of explanation, the Red Sea is divided  
151 into southern (13°N-18°N), central (18°N-23°N) and northern (23°N-28°N) regions and the seasons  
152 defined as winter (Dec-Feb), spring (Mar-Apr), summer (May-Aug) and fall (Sep-Nov).

### 153 **3 Results and discussion**

#### 154 **3.1 MLD variability in the Red Sea**

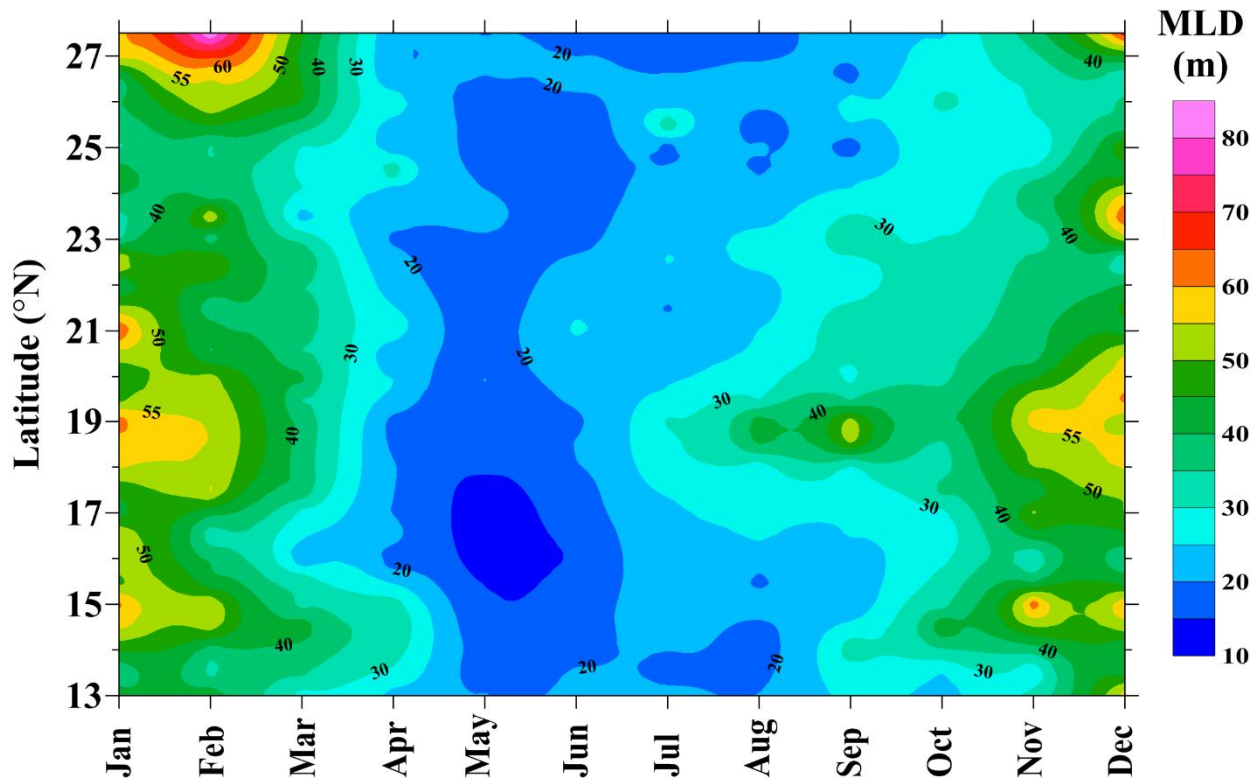
155 The Red Sea exhibits strong seasonal changes in its MLD, with deeper mixed layers during the winter  
156 and shallower ones during the summer, with gradual changes from deeper to shallower and vice versa in  
157 the transitional months. A Hovmoller diagram of the monthly MLD climatology is presented in Fig. 3.

158 The deepest MLD is observed in February and the shallowest during May-Jun. A significant annual  
159 variability is observed in the Red Sea. The maximum value of climatological mean MLD is observed in  
160 February at the northern Red Sea while the minimum noticed at various instances, especially during  
161 summer months. The MLD of individual profiles in the northern Red Sea has a wide range values from  
162 40 to 120 m mainly due to the presence of active convection process, while some of the profiles show  
163 MLD deeper than 150 m in consistence with Yao et al., (2014b).

164 In addition, the southern central Red Sea (14°N-21°N) also experienced deeper MLDs during winter. The  
165 observed shallow MLD patches are not considered because the noise in MLD ( $\sim 44 \pm 14$ m) is overlapping  
166 with mean MLD of northern ( $\sim 53$ m) and southern ( $\sim 48$ m) grids. The observed noise around 25°N is  
167 relatively small ( $\sim 30 \pm 9$  m) comparing to the difference in MLD values towards northern ( $\sim 70$ m) and  
168 southern ( $\sim 50$ m) latitudes, and hence this is considered as a shallow MLD region.

169 During July to September, the region around 19°N experienced a deeper mixed layer in contrast with the  
170 general pattern of summer shoaling over the entire Red Sea. The deepening of the MLD begins in October  
171 throughout the Red Sea. The winter cooling and associated convection strengthens by December, with  
172 an average MLD  $> 50$  m, which intensifies by January and persists throughout February.

173



174

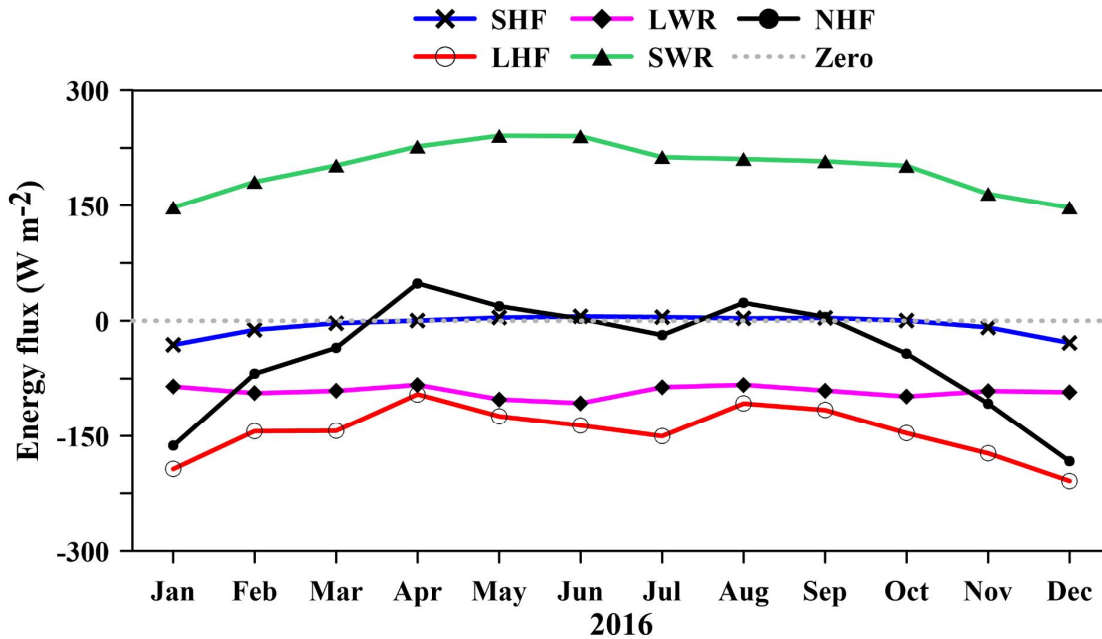
175 **Figure 3.** Hovmoller diagram of the MLD climatology along the axis of Red Sea.

176 The mixed layer starts to shoal gradually by the end of February, and the MLDs of most areas decreases  
 177 to  $20 \pm 7$  m by April. Summer shoaling is comparatively stronger in the  $15^{\circ}\text{N}$ - $18^{\circ}\text{N}$  latitude band, and the  
 178 detected mean MLD is  $< 15$  m. Individual observations revealed that many profiles have MLDs  $< 5$  m.  
 179 In general, the shallow mixed layers are predominant from April to September, while this prevails until  
 180 October in the far north. In the south-central Red Sea, the shallow mixed layer exists for only a short  
 181 period, from April to June.

182 **3.2 Major forces controlling the MLD variability**

183 MLD is directly influenced by changes in the net heat flux (NHF), fresh-water flux (E-P) and wind stress.  
 184 The different terms that contribute to NHF are given in Fig. 4 for a sample year 2016 in the central Red  
 185 Sea. On an annual average basis, the incoming shortwave radiation (SWR,  $202 \text{ W m}^{-2}$ , positive

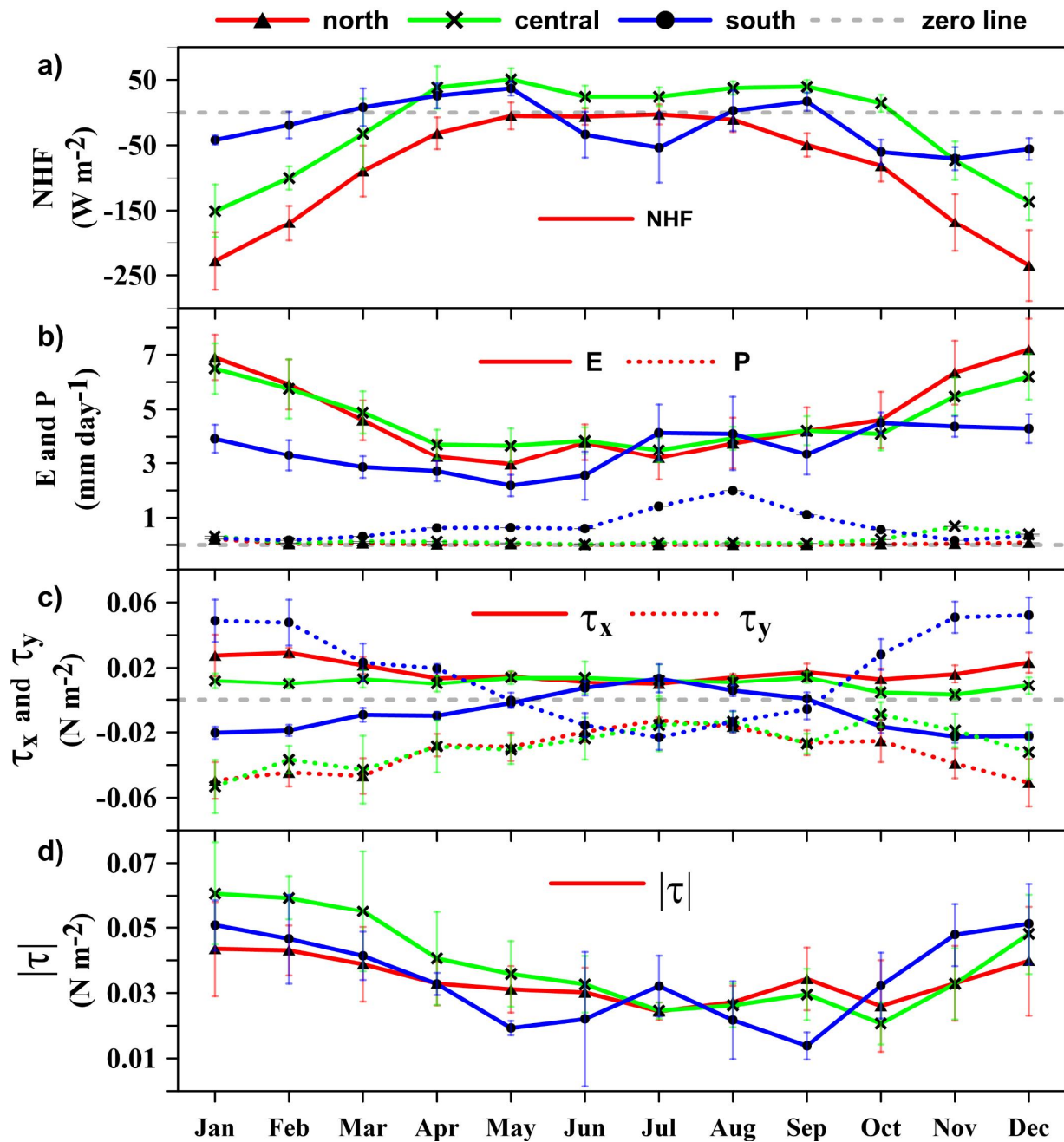
186 downward) is mainly balanced by LHF (latent heat flux,  $-126 \text{ W m}^{-2}$ ) and LWR (long wave radiation, -  
 187  $83 \text{ W m}^{-2}$ ), while the SHF (sensible heat flux) is only  $-4 \text{ W m}^{-2}$ . The net heat loss in the central Red Sea  
 188 is  $11 \text{ W m}^{-2}$ . Both the LHF and LWR are gradually increasing towards the northern Red Sea. The monthly  
 189 climatology of the NHF in the northern, central and southern Red Sea are given in Fig. 5a. Heat loss rises  
 190 above  $200 \text{ W m}^{-2}$  during December-January in the northern Red Sea, with a maximum of  $\sim 250 \text{ W m}^{-2}$  at  
 191 the northern end of the sea in December. The annual mean of NHF is negative (heat loss) across the Red  
 192 Sea, except for isolated locations in the southern Red Sea with trivial heat gain (figure not shown). The  
 193 thermal components of the buoyancy forces calculated based on Eq. (1) show that the heat flux support  
 194 mixing through buoyancy loss in the northern and central Red Sea during the winter, while it opposes  
 195 vertical mixing due to buoyancy gain during summer. In the southern Red Sea, the effect of heat flux is  
 196 relatively weak.



197

198 **Figure 4.** Time series of heat flux components (incoming shortwave radiation (SWR), long wave  
 199 radiation (LWR), latent heat flux (LHF), sensible heat flux (SHF) and net heat flux (NHF)) for the year  
 200 2016 in the central Red Sea.

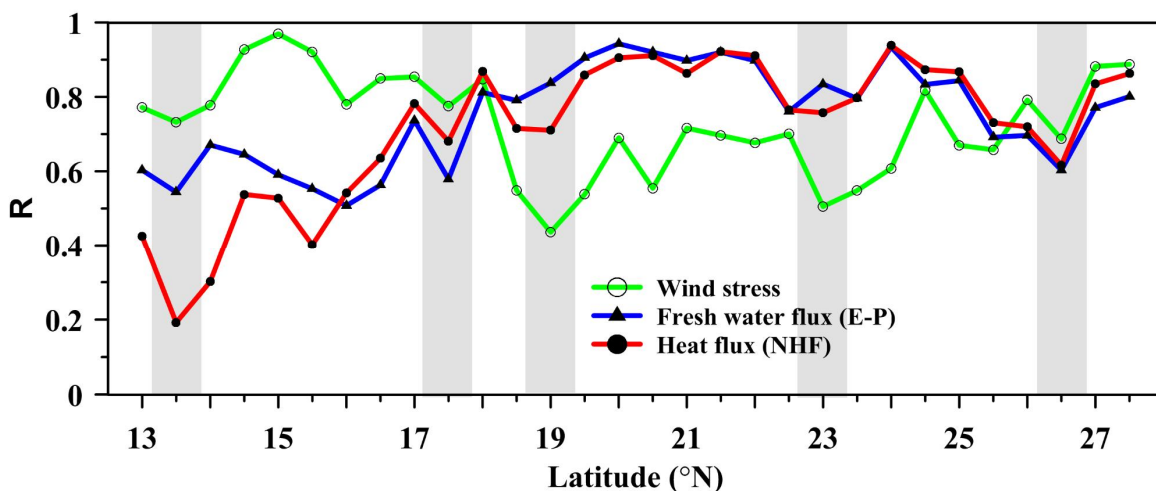
201 The evaporation rate in the Red Sea gradually increases from south to north (Fig. 5b). The central and  
202 northern Red Sea have higher evaporations during the winter ( $\sim 6 \text{ mm day}^{-1}$ ) and moderate evaporations  
203 ( $\sim 3 \text{ mm day}^{-1}$ ) during the summer. Evaporation shows weak seasonality in the southern Red Sea.  
204 Precipitation in the southern region is higher than those of the other areas of Red Sea, with maximum  
205 rainfall during July-September (Fig. 5b). The changes in buoyancy forces corresponding to fresh-water  
206 flux (haline component) are estimated based on Eq. (1), which shows that the changes support vertical  
207 mixing throughout the year and over the entire Red Sea. The thermal component is relatively higher than  
208 the haline component, and the net buoyancy flux follows a more or less similar pattern of thermal  
209 buoyancy flux all along the Red Sea (figure not shown). The observed variability of the above-discussed  
210 parameters is consistent with findings from earlier studies (Albarakati and Ahmad, 2013; Sofianos et al.,  
211 2002; Tragou et al., 1999).



212

213 **Figure 5.** Monthly climatology of a) NHF, b) evaporation and precipitation, c) eastward ( $\tau_x$ ) and  
 214 northward ( $\tau_y$ ) component of wind-stress, and d) magnitude of the wind stress ( $|\tau|$ ). South, central and  
 215 north regions are represented by the changes at  $14^\circ\text{N}$ ,  $21^\circ\text{N}$  and  $27^\circ\text{N}$ .

216 The pattern of wind stress in the Red Sea is significantly different from the other parameters. The wind  
 217 stress is strong during the winter, leading to enhanced turbulence and mixing, while it is weak during the  
 218 summer, resulting in a shallower mixed layer (Fig. 5c,d). Apart from that, strong surface winds blow to  
 219 the Red Sea through the Tokar gap at approximately 19°N in July and August.



220

221 **Figure 6.** Correlation between major forces and MLD. Shaded regions represent locations of coinciding  
 222 drops in correlation.

223 The correlations between MLDs and forcing factors are given in Fig. 6. The statistical significance of the  
 224 correlation values are verified based on t-test following (Bretherton et al., 1999), and the estimated p-  
 225 value, t-value and the effective degree of freedom show that the correlation values are statistically  
 226 significant at 95%. The wind stress and E-P are positively correlated with MLD while the NHF is  
 227 negatively correlated since as NHF (into the ocean) increases, MLD decreases. For simplicity of the figure  
 228 (Fig. 6), the correlation values of all parameters are presented as positive. NHF and E-P are well correlated  
 229 (>0.8) with MLD in the central and northern Red Sea, and weakly correlated in the south. Wind stress has  
 230 a higher correlation (>0.8) to the south, while it is relatively weakly correlated in the central and northern  
 231 Red Sea. Toward the northern end, the wind stress gradually achieves a higher correlation.

232 The results from Fig. 5 and 6 indicate that the MLD variability of the Red Sea is dominated by wind stress  
233 in the southern part, NHF (heat flux) and evaporation play a major role in the central region, while all the  
234 three are influencing in the northern region. Remarkably, for all the above-discussed parameters,  
235 coinciding drops are observed in the correlations at approximately 13.5°N, 17.5°N, 19°N, 23°N, and  
236 26.5°N, which indicate the impact of additional forces like eddies and currents in regulating the MLD  
237 variability of the region.

238 Earlier studies have proved that the upper ocean is efficiently re-stratified by the ocean eddies which may  
239 significantly change the MLD. The resultant effect of eddy is largely dependent on the eddy amplitude.  
240 The mixing intensity is largest at the center of eddy and decays on average with increasing radial distance  
241 (Dewar, 1986; Fox-Kemper et al., 2008; Hausmann et al., 2017; Smith and Marshall, 2009). The observed  
242 results show that the mixing associated with eddies is dominating over the existing effect of wind stress  
243 and heat flux. CE diminishes mixing through upwelling of the subsurface water while AE enhances  
244 mixing through downwelling of the surface water (de Boyer Montegut et al., 2004; Chelton et al., 2004,  
245 2011; Dewar, 1986; Hausmann et al., 2017).

246 Satellite altimetry maps revealed the presence of multiple eddies in the Red Sea which are often confined  
247 to specific latitude bands (Clifford et al., 1997; Johns et al., 1999; Quadfasel and Baudner, 1993; Sofianos  
248 and Johns, 2007). Analyzing the SLA maps from 1992 to 2012, Zhan et al., (2014) reported the presence  
249 of multiple eddies with both polarities in the Red Sea. The number of identified eddies peaked at  
250 approximately 19.5°N and 23.5°N. The upwelling proxy constructed using MODIS SST in the northern  
251 Red Sea shows the presence of frequent upwelling events at approximately 26.5°N almost every year  
252 (Papadopoulos et al., 2015) indicating the presence of cyclonic eddy. The extent and time of the upwelling  
253 vary from year to year. In summary, significantly large number of eddies are noticed around 19.5°N,  
254 23.5°N and 26.5°N, which could be the possible reason for coinciding drops in the correlation around  
255 19°N, 23°N and 26.5°N.

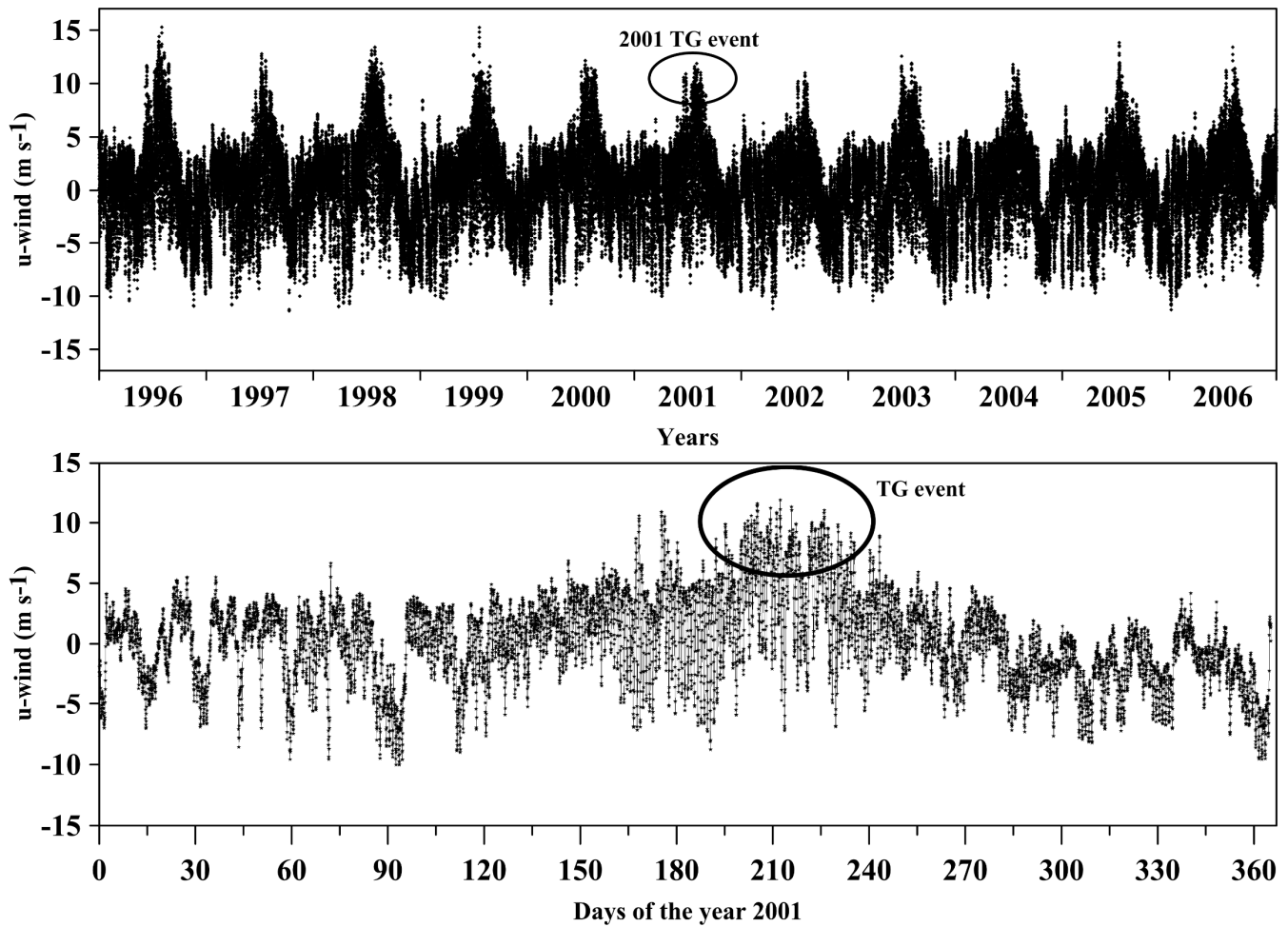
256 The Red Sea is very narrow at 13.5°N. Moreover, complex dynamics occur in this region associated with  
257 surface and subsurface currents in the strait between the Red Sea and the Gulf of Aden. The complexity  
258 of this region prevents linking the MLD variability directly to atmospheric forcing or eddies. The region



259 at approximately 17.5°N is between the two eddy-driven downwelling zones at approximately 15°N and  
260 19°N (Fig. 3). Mass conservation requires upwelling to replace the downwelling water. The MLD  
261 climatology shows shallow mixed layers throughout the year at 17.5°N, which could be due to possible  
262 upwelling. Further investigation is required to unveil the dynamics associated with this region.

### 263 **3.3 Influence of Tokar gap winds during the summer**

264 The Tokar gap is one of the largest gaps in the high orography located on the African coast of the Red  
265 Sea, near 19°N. Strong winds are funneled to the Red Sea through this gap which last for few days to  
266 weeks. Figure 7a shows the u-component of CFSR hourly surface wind at the Tokar region from 1996 to  
267 2006. From the figure, it shows that the strong wind events occur during summer every year while the  
268 intensity and duration of the event varies from year to year. Tokar gap winds frequently attain a speed of  
269  $15 \text{ m s}^{-1}$ . Previous research also show similar results (Jiang et al., 2009; Ralston et al., 2013; Zhai and  
270 Bower, 2013). Zhai and Bower (2013) reported that wind speed may reach 20 to  $25 \text{ m s}^{-1}$  based on ship-  
271 based observations. Figure 7b show that the onset of 2001 Tokar event was on 20<sup>th</sup> July and continued till  
272 20<sup>th</sup> August, where the maximum wind speed occurred during this period compared to rest of the year.  
273 These strong winds generate strong turbulence in the surface water, which enhances vertical mixing.

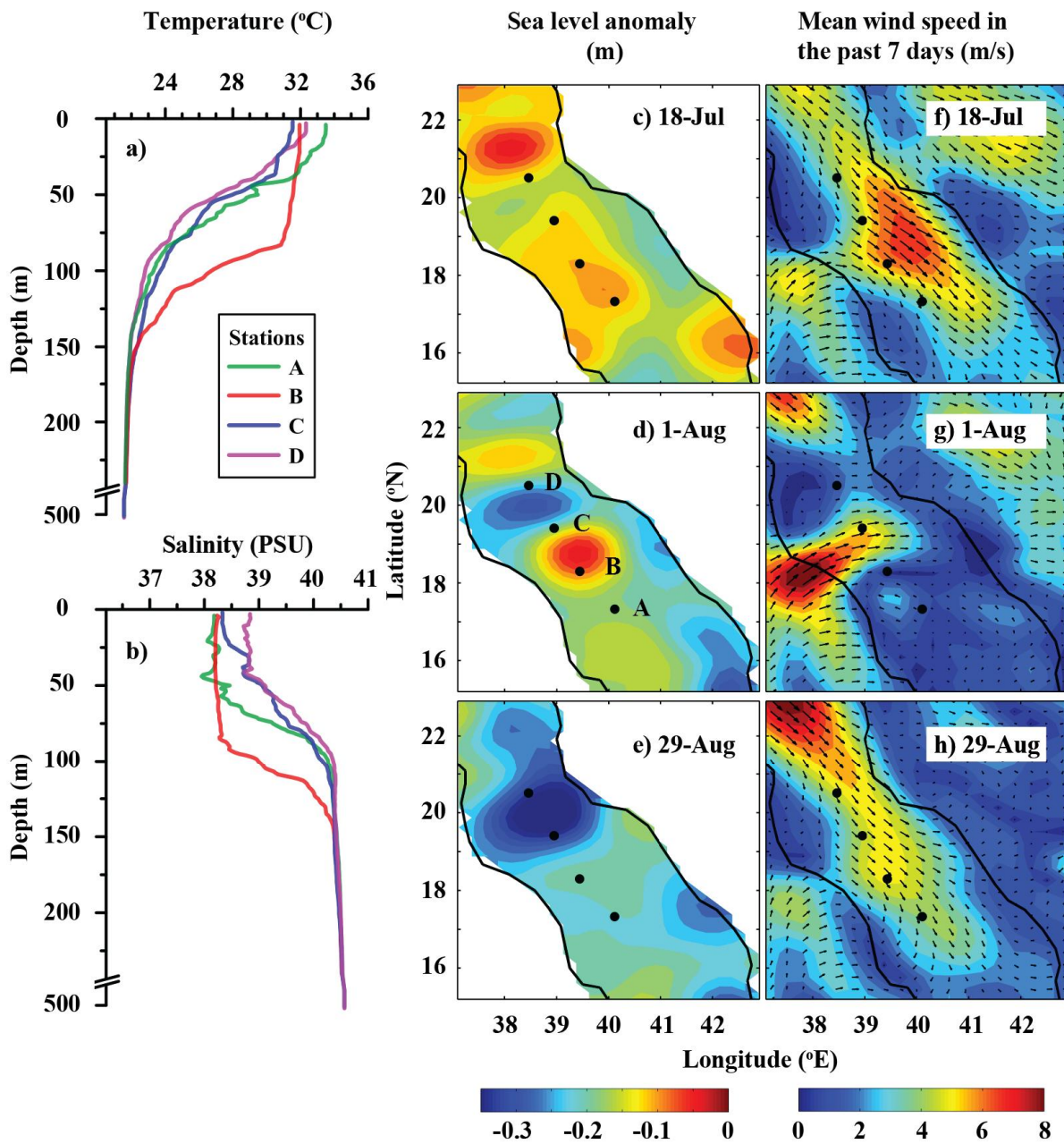


274

275 **Figure 7.** U-component of the CFSR hourly surface wind near the Tokar region (38.5°E, 18.5°N) a) from  
 276 year 1996 to 2006 and b) for the year 2001. The ellipse indicates the TG event in the year 2001.

277 The temperature and salinity profiles measured during summer 2001 (13-14 Aug 2001), which coincided  
 278 with the Tokar event are shown in Fig. 8a-b (Sofianos and Johns, 2007; Zhai and Bower, 2013). The  
 279 signature of Tokar event is clearly visible in the satellite-derived SLA, with well-defined cyclonic and  
 280 anticyclonic eddies to the north and south of the Tokar gap respectively (Fig. 8c-e). Both eddies have  
 281 basin-wide influence and radii between 70-80 km. Corresponding wind speed pattern (averaged for the  
 282 previous 7 days) is shown (Fig. 8f-h). The profiles to the north and south of the jet axis display a  
 283 significant difference in MLD, with a deeper mixed layer in the south. Station A is far from both cyclonic

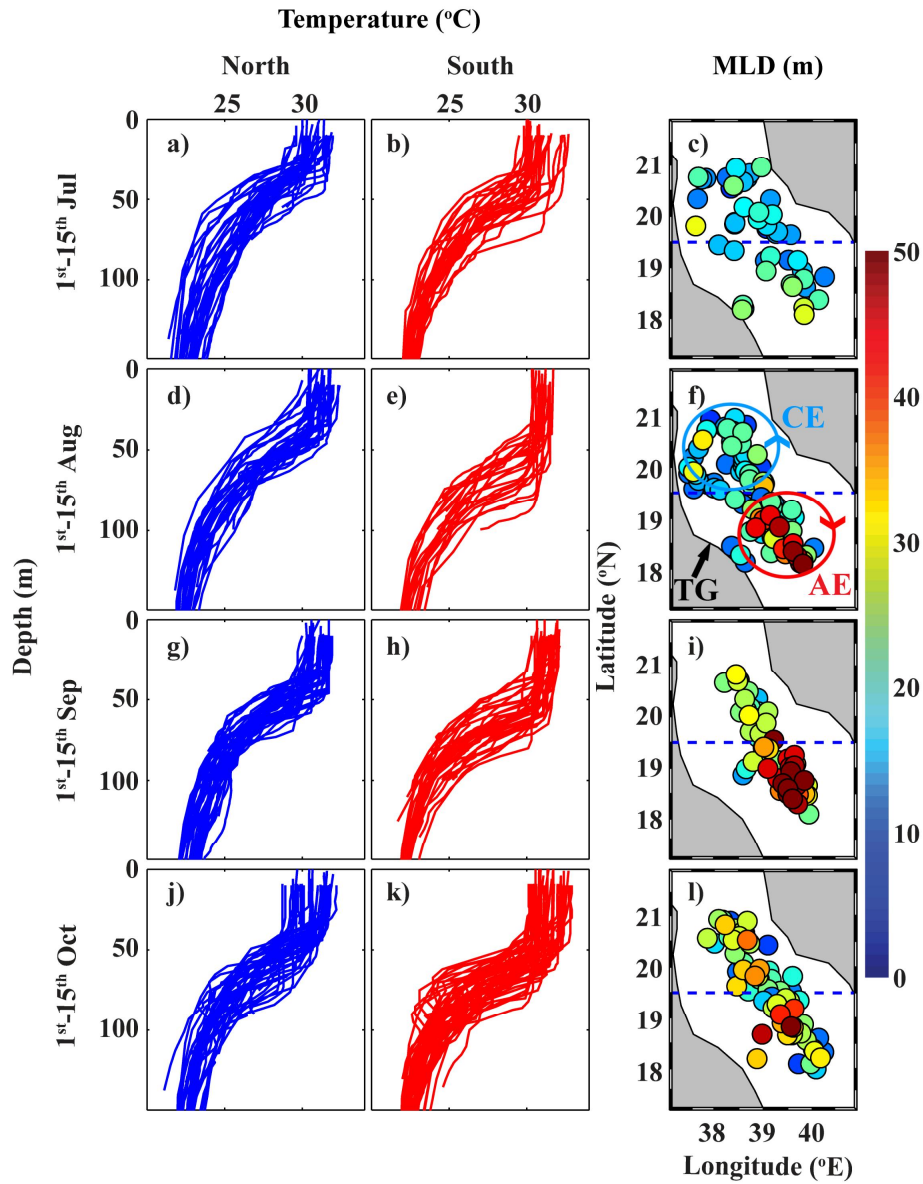
284 and anticyclonic eddies and shows the expected MLD during this period. The presence of the anticyclonic  
285 eddy at station B enhances strong downwelling, extending the mixing to a depth of approximately 80 m.  
286 It is to be noted that the entire Red Sea basin is well stratified during this period, with MLDs ranging  
287 from 10 m to 15 m. Stations C and D are located at the edge of the cyclonic eddy, and both have shallower  
288 thermocline and mixed layer.



289

290 **Figure 8.** (a) The CTD measured temperature and salinity profiles during 13-14 Aug 2001. (b) SLA maps  
 291 and (c) wind speed and direction (averaged for the previous one week) in the Tokar region, before, during  
 292 and after the Tokar event. The temperature and salinity profiles are received through personal  
 293 communication from (Sofianos and Johns, 2007).

294 The MLDs of all the available profiles in the Tokar region before, during, just after and after a month of  
295 the Tokar event are plotted in Fig. 9 (profiles for the first 15 days of each month are displayed). The mean  
296 MLD, standard deviation and number of profiles are given in Table 1. Before the Tokar event, the southern  
297 and northern sides of the Tokar axis ( $18^{\circ}\text{N}$ - $19.5^{\circ}\text{N}$  and  $19.5^{\circ}\text{N}$ - $21^{\circ}\text{N}$ , respectively) displayed similar  
298 mixed layers (Fig. 9a-c). During the Tokar event, the southern side experienced enhanced mixing, while  
299 the northern side show shallow mixed layer (Fig. 9d-f).



300

301 **Figure 9.** Temperature profiles from the north of the Tokar axis (left panel, blue curves), south of the  
 302 Tokar axis (middle panel, red curves) and the corresponding MLD (right panel) during the first 15 days  
 303 of each month from July to October. The dashed line passes through 19.5°N, roughly separating the north  
 304 and south of the Tokar axis. MLD of each profile is represented by the filled colors. The blue and red  
 305 circles in (f) schematically represent cyclonic and anticyclonic eddies during Tokar event, respectively.

306 **Table 1.** The mean MLD in the north and south of Tokar jet axis from July to October.

1-15 <sup>th</sup> days of the Month	Mean		Standard deviation		Number of profiles	
	North	South	north	south	north	south
<b>Jul (before)</b>	20	26	5	8	19	12
<b>Aug (during)</b>	24	38	8	17	27	24
<b>Sep (just after)</b>	30	52	11	14	27	27
<b>Oct (after one month)</b>	31	34	9	12	36	30

307 The anticyclonic part of the Tokar induced eddies enhances downwelling and the associated deepening  
 308 of the mixed layer along the southern side of the jet axis, while the cyclonic eddies generate upwelling  
 309 and the associated shoaling of the mixed layer along the northern side. The profiles in September (just  
 310 after the Tokar event) show the southern side is well mixed by the event, which leads to an average  
 311 difference of 20 m in the MLDs between both sides of the Tokar axis (Fig. 9g-i). The signature of the  
 312 Tokar events in the MLDs (MLD difference between north and south of the jet axis) has disappeared by  
 313 October (one month after the Tokar event, Fig. 9j-l). The dominant effect of mountain gap winds on MLD  
 314 changes has been reported in many studies globally, for instance, Gulfs of Tehuantepec in the Eastern  
 315 Tropical Pacific (Gonzalez-Silvera et al., 2004; Stumpf, 1975) and Bora in the Mediterranean Sea  
 316 (Grisogono and Belusic, 2009).

317 The mixing in the Tokar region during summer is the sum of the two mechanisms, the wind-induced  
318 turbulent mixing and the secondary circulation (eddies) induced by the wind. Both mechanisms act in the  
319 same direction in the southern side of the jet axis resulting in enhanced mixing, while they act in opposite  
320 direction in the northern side leading to reduced mixing. Further studies are required for proper  
321 quantification of the contribution of each mechanism. In summary, during the summer, the turbulence  
322 induced by strong wind and the impact of anticyclonic eddy enhance vertical mixing in the southern side  
323 of jet axis, while the wind-induced mixing is diminished by the presence of cyclonic eddy in the northern  
324 side of the jet axis.

#### 325 **4 Conclusions**

326 A detailed information on MLD variability is crucial for understanding the physical and biological  
327 processes in the ocean. The goals of this study were to produce a climatology record of MLD for the Red  
328 Sea and to investigate the role of major forces on MLD changes. With the help of in situ temperature  
329 profiles from CTD, XBT, MBT and profiler float measurements, the MLD variability in the Red Sea has  
330 been explored for the first time and the MLD climatology is produced for every 0.5 degrees along the  
331 main axis. The climatology reasonably captured all the major features of MLD variability in the Red Sea.  
332 The present work provides a climatological mean of the MLD structure in the Red Sea and its seasonal  
333 variability. Influences of wind stress, heat flux, evaporation and precipitation are explored. Further, the  
334 impact of the Tokar gap jet stream winds, the eddies and the upwelling events in the northern Red Sea are  
335 investigated.

336 A deep ventilation process associated with the winter cooling is observed across the entire Red Sea during  
337 the months of December to February (Fig. 3). Similarly, very shallow MLDs associated with increased  
338 short-wave radiation are detected all along the region from May to Jun. The climatological winter MLD  
339 ranges from ~40 to 85 m (in January). Similarly, the climatological summer MLD varies from 10 to ~20  
340 m (in June), which may reach to >40 (in July). The mixed layer becomes deeper toward the north, even  
341 though the pattern is not linear with increasing latitude. The largest amplitude of variability is observed  
342 at the tip of the northern Red Sea which is associated with strong deep convection during the winter and



343 shoaling during the summer. The region at approximately 19°N experienced deeper MLD than typical of  
344 elsewhere in the Red Sea. This region experienced enhanced mixing during winter by surface cooling,  
345 and during summer by both the Tokar gap wind induced turbulent mixing and the formation of the  
346 anticyclonic eddy. The deepest mixed layer is observed at the northern tip of Red Sea during the winter,  
347 but the deep nature of northern mixed layer is almost limited to the winter months.

348 Correlation analyses between MLD and forcing factors displayed the influence of major forces on MLD,  
349 from north to south of the Red Sea. In general, the wind stress mainly controls the MLD variability in the  
350 southern part of the Red Sea, heat flux and evaporation dominate in the central region, and all the three  
351 forces contribute in the northern region. Coinciding drops are observed in the correlations for all the  
352 selected forcing factors around the previously reported main eddy locations. In these locations, eddies  
353 override the controls of the other main forces, namely, wind stress, heat flux and fresh-water flux. The  
354 quasi-permanent cyclonic gyre and upwelling in the northern Red Sea lead to the shoaling of the mixed  
355 layer at ~26.5°N throughout almost the whole year.

356 The anticyclonic eddy induced by Tokar gap winds, and the wind induced turbulent mixing together  
357 enhanced the deep convection and mixing along the southern side of the Tokar jet axis during the summer,  
358 while the wind induced mixing is reduced by the cyclonic eddy. This leads to a deepening of the mixed  
359 layer, to >40 m, while the MLDs in the rest of the Red Sea are <20 m. The effect of Tokar event is seen  
360 in the profiles of late July to early August which gradually disappeared by October. The frequent eddies,  
361 associated with surface circulation and Tokar events, have a strong impact on the MLD structure of the  
362 Red Sea.

### 363 **Data availability**

364 The climatology data produced in this manuscript is available from the repository "Figshare"  
365 (DOI:10.6084/m9.figshare.5539852). The monthly mean values of heat fluxes and wind stress data are  
366 available from Tropflux ([http://www.incois.gov.in/tropflux\\_datasets/data/monthly/](http://www.incois.gov.in/tropflux_datasets/data/monthly/)). The monthly mean  
367 values of evaporation are accessible from OAflux

368 ([ftp://ftp.who.edu/pub/science/oaflux/data\\_v3/monthly/evaporation/](ftp://ftp.who.edu/pub/science/oaflux/data_v3/monthly/evaporation/)). The precipitation data is available  
369 from TRMM (<https://pmm.nasa.gov/data-access/downloads/trmm>).

### 370 **Acknowledgments**

371 This project was funded by the Deanship of Scientific Research (DSR), King Abdulaziz University, under  
372 grant number (438/150/129). The authors, therefore, acknowledge the DSR's technical and financial  
373 support. The authors acknowledge TropFlux, OAFlux, TRMM, AVISO, CFSR, World Ocean Database  
374 and Coriolis data center for making their data products publicly available. The authors also acknowledge  
375 the institutes who have provided CTD profiles from different cruises. The author CPA acknowledges the  
376 Deanship of Graduate Studies, King Abdulaziz University, Jeddah, for providing a Ph.D. Fellowship.

### 377 **References**

378

379

380 Abdulla, C. P., Alsaafani, M. A., Alraddadi, T. M. and Albarakati, A. M.: Estimation of Mixed Layer  
381 Depth in the Gulf of Aden: A New Approach, PLoS One, 11(10), e0165136,  
382 doi:10.1371/journal.pone.0165136, 2016.

383 Aboobacker, V. M., Shanas, P. R., Alsaafani, M. A. and Albarakati, A. M.: Wave energy resource  
384 assessment for Red Sea, Renew. Energy, 1–13, doi:10.1016/j.renene.2016.09.073, 2016.

385 Albarakati, A. M. and Ahmad, F.: Variation of the surface buoyancy flux in the Red Sea, Indian J. Mar.  
386 Sci., 42(6), 717–721, 2013.

387 Alsaafani, M. A. and Shenoi, S. S. C.: Seasonal cycle of hydrography in the Bab el Mandab region,  
388 southern Red Sea, J. Earth Syst. Sci., 113(3), 269–280, doi:10.1007/BF02716725, 2004.

- 389 Alsaafani, M. A. and Shenoi, S. S. C.: Water masses in the Gulf of Aden, *J. Oceanogr.*, 63(1), 1–14,  
390 doi:10.1007/s10872-007-0001-1, 2007.
- 391 Beal, L. M., Field, A. and Gordon, A. L.: Spreading of Red Sea overflow waters in the Indian Ocean, *J.*  
392 *Geophys. Res.*, 105(C4), 8549–8564, doi:10.1029/1999JC900306, 2000.
- 393 Bower, A. S. and Farrar, J. T.: Air-sea interaction and horizontal circulation in the Red Sea, in *The Red*  
394 *Sea*, pp. 329–342, Springer., 2015.
- 395 Boyer, T. P. and Levitus, S.: Quality control and processing of historical temperature, salinity, and  
396 oxygen data, NOAA Tech. Rep., NESDIS 81, 65, 1994.
- 397 de Boyer Montegut, C., Madec, G., Fischer, A. S., Lazar, A. and Iudicone, D.: Mixed layer depth over  
398 the global ocean: An examination of profile data and a profile-based climatology, *J. Geophys. Res. C*  
399 *Ocean.*, 109(12), 1–20, doi:10.1029/2004JC002378, 2004.
- 400 Bretherton, C. S., Widmann, M., Dymnikov, V. P., Wallace, J. M. and Bladé, I.: The Effective Number  
401 of Spatial Degrees of Freedom of a Time-Varying Field, *J. Clim.*, 12(7), 1990–2009, doi:10.1175/1520-  
402 0442(1999)012<1990:TENOSD>2.0.CO;2, 1999.
- 403 Carlson, D. F., Fredj, E. and Gildor, H.: The annual cycle of vertical mixing and restratification in the  
404 Northern Gulf of Eilat/Aqaba (Red Sea) based on high temporal and vertical resolution observations,  
405 *Deep. Res. Part I Oceanogr. Res. Pap.*, 84, 1–17, doi:10.1016/j.dsr.2013.10.004, 2014.
- 406 Chelton, D. B., Schlax, M. G., Freilich, M. H. and Milliff, R. F.: Satellite measurements reveal  
407 persistent small-scale features in ocean winds, *Science (80-. )*, 303(5660), 978–983, 2004.
- 408 Chelton, D. B., Schlax, M. G. and Samelson, R. M.: Global observations of nonlinear mesoscale eddies,  
409 *Prog. Oceanogr.*, 91(2), 167–216, doi:10.1016/j.pocean.2011.01.002, 2011.

- 410 Chen, D., Busalacchi, A. J. and Rothstein, L. M.: The roles of vertical mixing, solar radiation, and wind  
411 stress in a model simulation of the sea surface temperature seasonal cycle in the tropical Pacific Ocean,  
412 *J. Geophys. Res.*, 99(C10), 20345, doi:10.1029/94JC01621, 1994.
- 413 Cheng, L., Zhu, J., Cowley, R., Boyer, T. P. and Wijffels, S.: Time, probe type, and temperature  
414 variable bias corrections to historical expendable bathythermograph observations, *J. Atmos. Ocean.  
415 Technol.*, 31(8), 1793–1825, doi:10.1175/JTECH-D-13-00197.1, 2014.
- 416 Clifford, M., Horton, C., Schmitz, J. and Kantha, L. H.: An oceanographic nowcast/forecast system for  
417 the Red Sea, *J. Geophys. Res. Ocean.*, 102(C11), 25101–25122, doi:10.1029/97JC01919, 1997.
- 418 D’Ortenzio, F., Iudicone, D., de Boyer Montegut, C., Testor, P., Antoine, D., Marullo, S., Santoleri, R.  
419 and Madec, G.: Seasonal variability of the mixed layer depth in the Mediterranean Sea as derived from  
420 in situ profiles, *Geophys. Res. Lett.*, 32(12), L12605, doi:10.1029/2005GL022463, 2005.
- 421 Dewar, W. K.: Mixed layers in Gulf Stream rings, *Dyn. Atmos. Ocean.*, 10(1), 1–29, 1986.
- 422 Ducet, N., LaTraon, P. Y. and Reverdin, G.: Global high-resolution mapping of ocean circulation from  
423 TOPEX/Poseidon and ERS-1 and -2, *J. Geophys. Res. Ocean.*, 105(C8), 19477–19498,  
424 doi:10.1029/2000JC900063, 2000.
- 425 Fox-Kemper, B., Ferrari, R. and Hallberg, R.: Parameterization of Mixed Layer Eddies. Part I: Theory  
426 and Diagnosis, *J. Phys. Oceanogr.*, 38(6), 1145–1165, doi:10.1175/2007JPO3792.1, 2008.
- 427 Gonzalez-Silvera, A., Santamaria-del-Angel, E., Millán-Nuñez, R. and Manzo-Monroy, H.: Satellite  
428 observations of mesoscale eddies in the Gulfs of Tehuantepec and Papagayo (Eastern Tropical Pacific),  
429 *Deep Sea Res. Part II Top. Stud. Oceanogr.*, 51(6–9), 587–600, doi:10.1016/j.dsr2.2004.05.019, 2004.
- 430 Grisogono, B. and Belusic, D.: A review of recent advances in understanding the meso- and microscale

431 properties of the severe Bora wind, *Tellus A*, 61(1), 1–16, doi:10.1111/j.1600-0870.2008.00369.x,  
432 2009.

433 Hausmann, U., McGillicuddy, D. J. and Marshall, J.: Observed mesoscale eddy signatures in Southern  
434 Ocean surface mixed-layer depth, *J. Geophys. Res. Ocean.*, 122(1), 617–635,  
435 doi:10.1002/2016JC012225, 2017.

436 Jiang, H., Farrar, J. T., Beardsley, R. C., Chen, R. and Chen, C.: Zonal surface wind jets across the Red  
437 Sea due to mountain gap forcing along both sides of the Red Sea, *Geophys. Res. Lett.*, 36(19), 1–6,  
438 doi:10.1029/2009GL040008, 2009.

439 Johns, W. E., Jacobs, G. A., Kindle, J. C., Murray, S. P. and Carron, M.: Arabian marginal seas and  
440 gulfs. University of Miami RSMAS Technical Report., University of Miami, Florida, USA., 1999.

441 Kara, A. B., Rochford, P. A. and Hurlburt, H. E.: Mixed layer depth variability over the global ocean, *J.*  
442 *Geophys. Res.*, 108(C3), 3079, doi:10.1029/2000JC000736, 2003.

443 Keerthi, M. G., Dyn, C., Monte, C. D. B., Lengaigne, M., Vialard, J., Boyer Montégut, C.,  
444 Muraleedharan, P. M., Dyn, C., Monte, C. D. B., Keerthi, M. G., Lengaigne, M., Vialard, J., Boyer  
445 Montégut, C., Muraleedharan, P. M., de Boyer Montégut, C. and Muraleedharan, P. M.: Interannual  
446 variability of the Tropical Indian Ocean mixed layer depth, *Clim. Dyn.*, 40(3–4), 743–759,  
447 doi:10.1007/s00382-012-1295-2, 2012.

448 Keerthi, M. G., Lengaigne, M., Drushka, K., Vialard, J., Montegut, C. D. B., Pous, S., Levy, M. and  
449 Muraleedharan, P. M.: Intraseasonal variability of mixed layer depth in the tropical Indian Ocean, *Clim.*  
450 *Dyn.*, 46(7–8), 2633–2655, doi:10.1007/s00382-015-2721-z, 2016.

451 LaTraon, P. Y. and Dibarboure, G.: Mesoscale Mapping Capabilities of Multiple-Satellite Altimeter  
452 Missions, *J. Atmos. Ocean. Technol.*, 16(9), 1208–1223, doi:10.1175/1520-

453 0426(1999)016<1208:MMCOMS>2.0.CO;2, 1999.

454 Lorbacher, K., Dommenges, D., Niiler, P. P. and Köhl, A.: Ocean mixed layer depth: A subsurface  
455 proxy of ocean-atmosphere variability, *J. Geophys. Res. Ocean.*, 111(7), 1–22,  
456 doi:10.1029/2003JC002157, 2006.

457 Papadopoulos, V. P., Zhan, P., Sofianos, S. S., Raitsos, D. E., Qurban, M., Abualnaja, Y., Bower, A. S.,  
458 Kontoyiannis, H., Pavlidou, A., Asharaf, T. T. M., Zarokanellos, N. and Hoteit, I.: Factors governing  
459 the deep ventilation of the Red Sea, *J. Geophys. Res. Ocean.*, 120(11), 7493–7505,  
460 doi:10.1002/2015JC010996, 2015.

461 Polovina, J., Mitchum, G. T. and Evans, T.: Decadal and basin-scale variation in mixed layer depth and  
462 the impact on biological production in the Central and North Pacific , 1960-88, *Deep Sea Res.*, 42(10),  
463 1701–1716, 1995.

464 Praveen Kumar, B., Vialard, J., Lengaigne, M., Murty, V. S. N. and McPhaden, M. J.: TropFlux: air-sea  
465 fluxes for the global tropical oceans—description and evaluation, *Clim. Dyn.*, 38(7–8), 1521–1543,  
466 doi:10.1007/s00382-011-1115-0, 2012.

467 Praveen Kumar, B., Vialard, J., Lengaigne, M., Murty, V. S. N., McPhaden, M. J., Cronin, M. F.,  
468 Pinsard, F. and Gopala Reddy, K.: TropFlux wind stresses over the tropical oceans: evaluation and  
469 comparison with other products, *Clim. Dyn.*, 40(7–8), 2049–2071, doi:10.1007/s00382-012-1455-4,  
470 2013.

471 Quadfasel, D. and Baudner, H.: Gyre-scale circulation cells in the red-sea, *Oceanol. Acta*, 16(3), 221–  
472 229, 1993.

473 Ralston, D. K., Jiang, H. and Farrar, J. T.: Waves in the Red Sea: Response to monsoonal and mountain  
474 gap winds, *Cont. Shelf Res.*, 65, 1–13, doi:10.1016/j.csr.2013.05.017, 2013.

475 Saha, S., Moorthi, S., Pan, H. L., Wu, X., Wang, J., Nadiga, S., Tripp, P., Kistler, R., Woollen, J.,  
476 Behringer, D., Liu, H., Stokes, D., Grumbine, R., Gayno, G., Wang, J., Hou, Y. T., Chuang, H. Y.,  
477 Juang, H. M. H., Sela, J., Iredell, M., Treadon, R., Kleist, D., Van Delst, P., Keyser, D., Derber, J., Ek,  
478 M., Meng, J., Wei, H., Yang, R., Lord, S., Van Den Dool, H., Kumar, A., Wang, W., Long, C.,  
479 Chelliah, M., Xue, Y., Huang, B., Schemm, J. K., Ebisuzaki, W., Lin, R., Xie, P., Chen, M., Zhou, S.,  
480 Higgins, W., Zou, C. Z., Liu, Q., Chen, Y., Han, Y., Cucurull, L., Reynolds, R. W., Rutledge, G. and  
481 Goldberg, M.: The NCEP climate forecast system reanalysis, *Bull. Am. Meteorol. Soc.*, 91(8), 1015–  
482 1057, doi:10.1175/2010BAMS3001.1, 2010.

483 Shanas, P. R., Aboobacker, V. M., Albarakati, A. M. A. and Zubier, K. M.: Climate driven variability of  
484 wind-waves in the Red Sea, *Ocean Model.*, 119, 105–117, doi:10.1016/j.ocemod.2017.10.001, 2017.

485 Smith, K. S. and Marshall, J.: Evidence for Enhanced Eddy Mixing at Middepth in the Southern Ocean,  
486 *J. Phys. Oceanogr.*, 39(1), 50–69, doi:10.1175/2008JPO3880.1, 2009.

487 Sofianos, S. S. and Johns, W. E.: An Oceanic General Circulation Model (OGCM) investigation of the  
488 Red Sea circulation, 1. Exchange between the Red Sea and the Indian Ocean, *J. Geophys. Res.*,  
489 107(C11), 3196, doi:10.1029/2001JC001184, 2002.

490 Sofianos, S. S. and Johns, W. E.: Observations of the summer Red Sea circulation, *J. Geophys. Res.*  
491 *Ocean.*, 112(6), 1–20, doi:10.1029/2006JC003886, 2007.

492 Sofianos, S. S., Johns, W. E. and Murray, S. P.: Heat and freshwater budgets in the Red Sea from direct  
493 observations at Bab el Mandeb, *Deep. Res. Part II Top. Stud. Oceanogr.*, 49(7–8), 1323–1340,  
494 doi:10.1016/S0967-0645(01)00164-3, 2002.

495 Stumpf, H. G.: Satellite Detection of Upwelling in the Gulf of Tehuantepec, Mexico, *J. Phys.*  
496 *Oceanogr.*, 5(2), 383–388, doi:10.1175/1520-0485(1975)005<0383:SDOUIT>2.0.CO;2, 1975.

497 Sutton, P. J., Worcester, P. F., Masters, G., Cornuelle, B. D. and Lynch, J. F.: Ocean mixed layers and  
498 acoustic pulse propagation in the Greenland Sea, *J Acoust Soc Am*, 94(3), 1517–1526,  
499 doi:10.1121/1.408130, 2014.

500 Tragou, E., Garrett, C., Outerbridge, R. and Gilman, C.: The Heat and Freshwater Budgets of the Red  
501 Sea, *J. Phys. Oceanogr.*, 29(10), 2504–2522, doi:10.1175/1520-  
502 0485(1999)029<2504:THAFBO>2.0.CO;2, 1999.

503 Turner, J. S.: *Buoyancy Effects in Fluids*, Cambridge University Press, Cambridge., 1973.

504 Yao, F., Hoteit, I., Pratt, L. J., Bower, A. S., Zhai, P., Köhl, A. and Gopalakrishnan, G.: Seasonal  
505 overturning circulation in the Red Sea: 1. Model validation and summer circulation, *J. Geophys. Res.*  
506 *Ocean.*, 119(4), 2238–2262, doi:10.1002/2013JC009004, 2014a.

507 Yao, F., Hoteit, I., Pratt, L. J., Bower, A. S., Köhl, A., Gopalakrishnan, G. and Rivas, D.: Seasonal  
508 overturning circulation in the Red Sea: 2. Winter circulation, *J. Geophys. Res. Ocean.*, 119(4), 2263–  
509 2289, doi:10.1002/2013JC009331, 2014b.

510 Zeng, L. and Wang, D.: Seasonal variations in the barrier layer in the South China Sea: characteristics,  
511 mechanisms and impact of warming, *Clim. Dyn.*, 48(5–6), 1911–1930, doi:10.1007/s00382-016-3182-  
512 8, 2017.

513 Zhai, P. and Bower, A. S.: The response of the Red Sea to a strong wind jet near the Tokar Gap in  
514 summer, *J. Geophys. Res. Ocean.*, 118(1), 422–434, doi:10.1029/2012JC008444, 2013.

515 Zhan, P., Subramanian, A. C., Yao, F. and Hoteit, I.: Eddies in the Red Sea: A statistical and dynamical  
516 study, *J. Geophys. Res. Ocean.*, 119(6), 3909–3925, doi:10.1002/2013JC009563, 2014.

517